SAND2015-5544C

Mesoscale Modeling and Simulation of Composition, Manufacturing, and Microstructure Effects on Electrical Conduction in Thermal Battery Cathodes

Emilee L. Reinholz[a,b], Scott A. Roberts[a], P. Randall Schunk[a,b], Christopher A. Apblett[a,b]

[a] Sandia National Laboratories, Albuquerque, New Mexico, 87185 USA
[b] Department of Chemical and Biological Engineering, University of New Mexico, Albuquerque, New Mexico 87131, USA

Li/FeS_2 thermal batteries provide a stable, robust, and reliable power source capable of long-term electrical energy storage without performance degradation. These systems rely on the electrical conductivity of FeS_2 cathodes for critical performance parameters such as power and lifetime, and on permeability of the electrolyte through the solid FeS_2 particles for ion transfer. The effects of component composition, manufacturing conditions, and the mechanical deformation on conductivity and permeability have not been studied. We present simulation results from a finite element computer model compared with impedance spectroscopy electrical conductivity experiments. Our methods elucidate the combined effects of slumping, particle size distribution, composition, and pellet density on properties related to electrical conduction in Li/FeS_2 thermal battery cathodes.

Introduction

When heated, the salt in Li/FeS_2 thermal battery cathodes melt, forming a suspension. This suspension then deforms, leading to bulk mechanical deformation, or “slumping." Slumping causes changes to the mechanical compression, tortuosity, permeability, electronic conductivity, and ionic conductivity of each cell as the microstructure reorganizes in response to external compression of the cell stack. The effect of this behavior upon cathode electrical and flow properties is of critical importance to battery performance parameters, such as power and lifetime (1, 2, 3). Yet, the combined effect of slumping, cathode composition, and cathode manufacturing conditions has not been investigated, although aspects have been studied individually.

Cathode composition and manufacturing conditions influence battery performance directly. The FeS_2 particle size distribution affects battery activated life (4); run time and capacity (5); and energy density, thermal stability, and specific energy (6, 7). In addition, pellet density relates to cell reactivity (7). A study of the ratio of FeS_2 quantities with respect to other components remains less understood. The processing-microstructure-property-performance relationship requires further investigation, especially with respect to the link between slumping behavior and material properties.

Here we present a joint computational and experimental effort to better understand how these combined effects influence the electrical conductivity and permeability of Li/FeS_2 thermal battery cathodes. We follow a computational approach very similar to that of Roberts et al. (8), where the finite element method was applied to a realistic geometric

representation of an electrode microstructure, reconstructed from three-dimensional experimental characterization. In this paper, we begin with the geometric representation and the model setup. Next, we illustrate the application of the finite element method to the geometry. Then, we describe the experimental validation approach. Lastly, we present a brief description of the results, followed by the conclusion.

Microstructure Characterization and Geometry Reconstruction

Microstructure characterization was achieved with MicroCT using an Xradia 520 Versa 3D X-ray microscope (ZEISS, Jena, Germany). Two fractions of nine cathode pellet types were characterized, one before and one after slumping, for a total of eighteen characterizations. The Xradia system acquired a sample volume of greater than 0.1 mm^3 with 0.5 micron pixel size for each characterization. The raw X-ray projections were reconstructed and exported as a stack of TIFF files. Using Avizo software (15), we reconstructed the stack of TIFFs into a three-dimensional geometry, cropped the geometry, and applied a Watershed algorithm to threshold and segment the microstructure. We simplified the geometry to represent two phases within a cube: the FeS_2 phase, and a phase combining LiCl/KCl electrolyte, MgO binder, Li_2O lithiating agent, and pores (EBLP). Then the FeS_2 particle phase was isolated. A cross-section is shown in Fig. 1.

Model Setup

Electrical Conductivity

The effective electrical conductivity model is governed by the steady-state continuity equation for current density, where the divergence theorem equates the integrals in Eq. [1] (9). Ohm's law, Eq. [2], relates Eq. [1] to the local electrical conductivity (σ_e) (10). Integration or averaging of **J** over the domain gives the effective electrical conductivity. In these equations, **J** is the electrical current vector, **n** is the normal vector, **E** is the electric field vector, and V represents the potential.

$$-\oint_S \mathbf{J}\cdot\mathbf{n}\,\mathrm{dA} = \int -\nabla\cdot\mathbf{J}\,\mathrm{dV} = 0 \qquad [1]$$

$$\mathbf{J} = \sigma_e\mathbf{E} = -\sigma_e\nabla V \qquad [2]$$

Dirichlet boundary conditions were applied to find the upper bound of the effective electrical conductivity by the method described by Ostoja-Starzewski (11). At the left *yz* face of the cube, we specified 0 V, and at the right *yz* face, we specified 1 V (Figure 1). The electrical conductivity values were 10 $\Omega^{-1}\mathrm{m}^{-1}$ and 1×10^{-14} $\Omega^{-1}\mathrm{m}^{-1}$ for the FeS_2 and EBLP phases, respectively.

Permeability

Navier-Stokes equations govern the electrolyte permeability model (12). The form of the governing equations is that of Stokes, or creeping, flow. Stokes flow assumes an incompressible, small Reynolds number, homogeneous, Newtonian fluid with very slow flow through a rigid, porous medium with isothermal, steady-state conditions. The continuity equation and Navier-Stokes equations simplify to characterize Stokes flow, Eqs. [3-4]

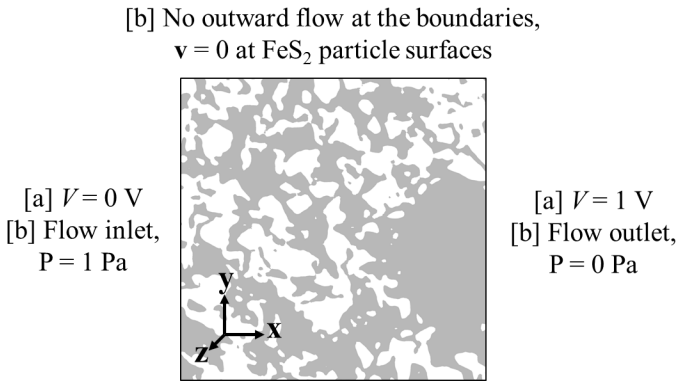

Figure 1: Setup for the [a] effective electrical conductivity and [b] permeability models. The FeS_2 (white) and EBLP (gray) phases are shown.

(13, 12). In this approximation, gravity is neglected due to horizontal flow. The equations below include the velocity vector ($\mathbf{v}$), viscosity (μ), pressure (P), the permeability scalar (κ), volumetric flow rate (Q), system length in the direction of flow (L_x), and cross-sectional area normal to the direction of flow (A_x).

$$\nabla \cdot \mathbf{v} = 0 \quad [3]$$

$$\mu \nabla^2 \mathbf{v} = \nabla P \quad [4]$$

Permeability is then calculated from the flow rate, found by taking a surface integral of the velocity for a cross-section normal to the direction of flow. The flow rate is applied to Darcy's law, Eq. [5] (13, 14). Darcy's law assumes isotropic flow properties.

$$\kappa = \frac{Q L_x \mu}{A_x \Delta P} \quad [5]$$

Dirichlet boundary conditions included outward flow at only the inlet and outlet and a no-slip boundary condition at all particle and electrolyte interfaces. Two additional flux boundary conditions specified the pressure at the inlet and outlet (1 Pa and 0 Pa, respectively) with free open flow pressure conditions. The electrolyte material properties were 1.5×10^3 kg/m^3 density and 1.5×10^{-3} PI viscosity, with incompressible Newtonian momentum stress. A simplified depiction of the setup is shown in Fig. 1.

CDFEM

The conformal decomposition finite element method (CDFEM) (16) is a novel code within Sierra Mechanics (10, 19, 18) used to model fluid transport when domains do not conform to a mesh. This algorithm describes the fluid domain with level set functions. CDFEM alters the non-conformal background mesh when it decomposes elements along the level set interfaces, followed by enrichment, during which nodes are added to the interfaces (Figure 2c). This process prevents issues such as mesh tangling in transient models, but also works effectively when modeling complicated geometries. CDFEM was selected for this research for to its ability to efficiently and effectively model the complicated geometries generated from our reconstructions of MicroCT data.

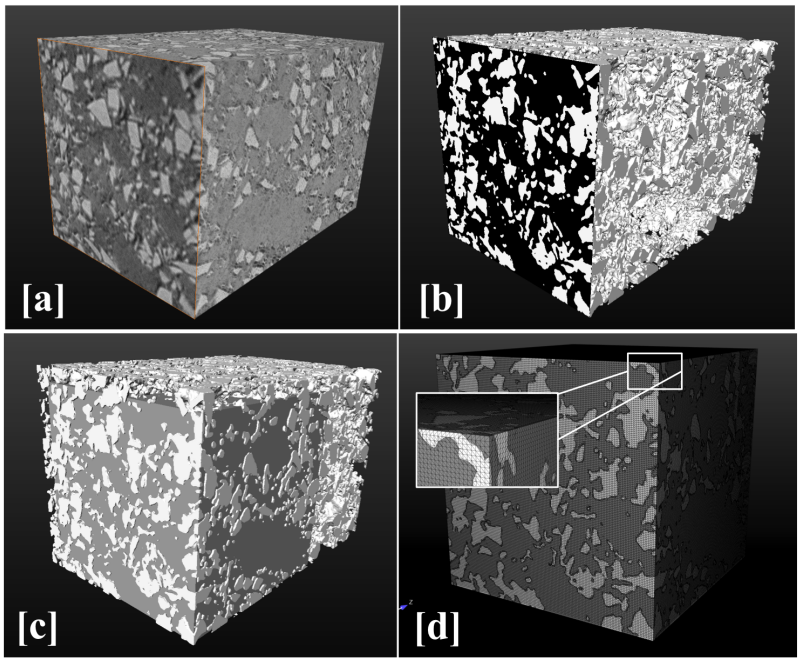

Figure 2: Workflow of MicroCT data to a computational mesh.
[a] Volume rendering of cropped MicroCT characterization. FeS_2 particles appear brighter than the EBLP phase.
[b] Thresholding and segmentation results, with FeS_2 particles shown (white).
[c] EBLP geometry (gray) position shown with respect to FeS_2 particles.
[d] Application of CDFEM to the combined FeS_2 and EBLP/background meshes.

Following the workflow for CDFEM (16) (Fig. 2), we generated a geometry to represent the EBLP phase. We generated a 0.027 mm^3 cubic geometry for the conductivity model, and a 0.012 mm^3 rectangular prism for the permeability model. We applied CUBIT (17) software to create and mesh the EBLP representative geometry with a tetrahedral mesh. Avizo generated a triangulated surface mesh on the FeS_2 particle phase.

We applied CDFEM to the FeS_2 surface mesh and the EBLP background ("fluid") mesh. The algorithm combined two meshes to form a conformal tetrahedral mesh. Then, Sierra mechanics solved the relevant equations described in the "Model Setup" section. Convergence requirements for all simulations included a 1×10^{-8} residual tolerance for the level set equation system and 1×10^{-12} residual tolerance for the conductivity and permeability equation systems. Each simulation ran until the convergence requirements were satisfied.

Experimental Data

Cathode Pellet Preparation

Nine pellet types with three parameter variations were manufactured in-house. The three parameters included the FeS_2 particle size distribution; ratio of FeS_2 to electrolyte, binder, and Li_2O; and pressed pellet density. Pellet formation followed with uniaxially

cold-pressing the cathode powders. All pellet and powder handling occurred in a humidity-controlled lab or an argon glove box to prevent moisture contamination.

Electrical Conductivity Measurements

Electrical conductivity measurements were performed with an SI 1287 Electrochemical Interface combined with an SE 1255 Frequency Response Analyzer (Solartron, Farnborough, England) and a custom single cell tester. In preparation for measurements, we assembled individual samples by sandwiching one cathode pellet between two thin stainless steel sheets of the pellet diameter and two outer layers of mica. Each sample assembly was placed into the tester, where each assembly was placed between two cylindrical temperature-controlled steel blocks and compressed uniaxially by a user-defined mass. Each assembly's stainless steel electrodes permitted electrical connections to the impedance spectroscopy equipment and the mica provided electrical insulation from the steel blocks.

Samples were compressed and heated to thermal equilibrium at three temperatures (25, 100, and 200°C), and tested with impedance spectroscopy before and after slumping at 500°C. ZPlot software (20) fit each impedance spectrum (Fig. 3) to an idealized circuit with a single resistor (R_{fit}) because all samples displayed purely resistive behavior, indicated by a phase shift, or theta, near zero (21). We calculated the conductivity (σ_e) for each sample using the pellet cross-sectional area (A) and thickness (l), as in Eq. [6].

$$\sigma_e = \frac{l}{R_{fit}A} \quad [6]$$

Results and Discussion

Electrical Conductivity, Model and Experiment

The electrical conductivity experimental results indicated that processing and composition parameters provide the greatest effect on conductivity prior to slumping. A forward stepwise regression model fit of the calculated preslumped conductivities and experimental parameters (particle size distribution, composition, and density) provided an R^2 value above 0.9, but a postslumped fit was unachievable, indicating a poor relationship between these parameters and postslumped conductivity. When considered for all pellet types with processing and composition parameters disregarded, slumping increases conductivity significantly, (Figure 3b). The model results fit well with the experimental results presented, where the conductivity increase due to slumping was nearly 40% different. An example of the results is shown in Figure 4a.

The lack of conductivity trend due to changes in the composition and processing likely indicates that the variations were too similar to make a noticeable difference. The significant effect due to slumping provides greater evidence that the microstructure reorganization enhances electron percolation, and thus electrical conductivity, through the cathode.

Electrolyte Permeability

Electrolyte flow was simulated through the microstructure of one cathode type prior

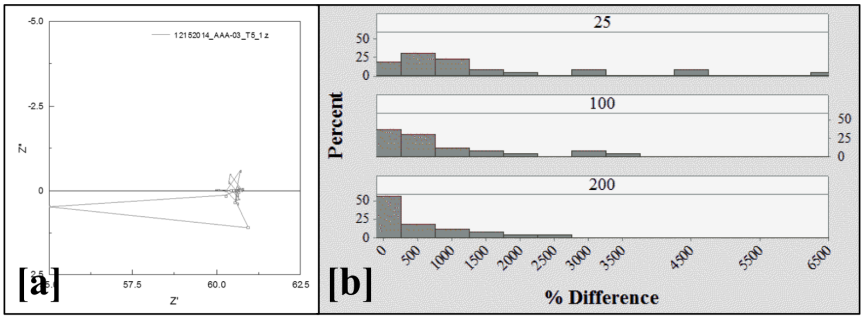

Figure 3: Experimental results.
[a] Impedance spectrum showed purely resistive behavior for all tests.
[b] Histogram summary of conductivity results: percent difference due to slumping at 25, 100, and 200°C.

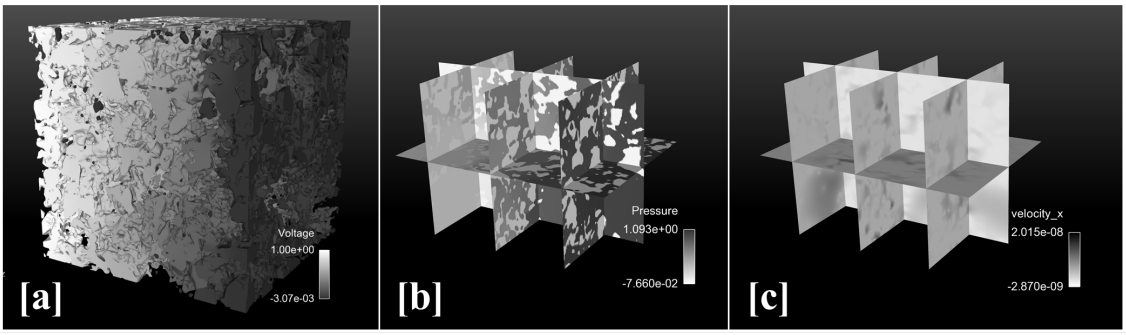

Figure 4: Simulation results.
[a] Electrical conductivity model, with voltage results shown for the FeS_2 particle phase.
[b-c] Electrolyte permeability model results for [b] fluid velocity and [c] pressure.

and after slumping. Before slumping, the permeability was approximately 2.73×10^{-12} m^2, and after slumping, the percent difference was greater than -40%. Literature values for sandstone, which has a comparable geometry, share the same order of magnitude, 10^{-10} to 10^{-13} m^2 (13).

Conclusions

We described a computational and experimental method to determine cathode properties critical for electrical conduction and ultimately, thermal battery performance. Experimentally, the combined impact of slumping, composition, and processing parameters upon cathode conductivity affected the preslumped conductivity more than the postslumped conductivity. Initial computational results showed a significant increase in electrical conductivity and a decrease in electrolyte permeability due to slumping. More extensive results of these simulations on all eigtheen MicroCT characterizations will provide a fuller understanding of the effects of processing parameters, composiiton, and slumping upon thermal battery cathode electrical conductivity and permeability.

Acknowledgements

The authors would like to thank David Noble, for help troubleshooting the input decks; Linda Johnson, for preparing the pellets; Lauren Wilson, for her assistance with statistical analysis; and Ryan Wixom, Barry Ritchey, and Burke Kernen for the MicroCT characterizations.

Sandia National Laboratories is a multi-program laboratory managed and operated by Sandia Corporation, a wholly owned subsidiary of Lockheed Martin Corporation, for the U.S. Department of Energy's National Nuclear Security Administration under contract DE-AC04-94AL85000.

References

1. R. Guidotti and P. Masset, *J. Power Sources*, **161**, 1443 (2006).
2. P. Masset and R. Guidotti, *J. Power Sources*, **177**, 595 (2008).
3. C. W. Wang, K. A. Cook, and A. M. Sastry, *J. Electrochem. Soc.*, **150**, A385 (2003).
4. R. Guidotti, F. W. Reinhardt, and W. F. Hammetter, *Sandia National Laboratories Tech. Report*, SAND 85-1737 (1988).
5. G. L. Di Benedetto, R. R. Carpenter, D. B. Swanson, and B. D. Wightman, Proceedings of the 46th Power Sources Conference, Orlando, FL (2014).
6. M. Au, *J. Power Sources*, **115**, 360 (2003).
7. C. M. Lamb, in *Linden's Handbook of Thermal Batteries, 4th Ed.*, Thomas Reddy, Editor, Ch. 36, McGraw-Hill, New York (2011).
8. S. A. Roberts, V. E. Brunini, K. N. Long, and A. M. Grillet, *J. Electrochem. Soc.*, **161**, F3052 (2014).
9. J. R. Reitz, F. J. Milford, and R. W. Christy, *Foundations of Electromagnetic Theory, 3rd Ed.*, p. 139, Addison-Wesley, Reading, MA (1979).
10. P. K. Notz, S.R. Subia, M. M. Hopkins, H. K. Moffat, and D. R. Noble, *Sandia National Laboratories Tech. Report*, SIERRA Multimechanics Module: Aria User Manual - Version 4.34 (2014).
11. M. Ostoja-Starzewski, *Phys. Rev. B*, **54**, 278 (1996).
12. S. P. Neumann, *Acta Mech.*, **25**, 153 (1977).
13. P. Mostaghimi, M. J. Blunt, and B. Bijeljic, *Math Geosci.*, **45**, 103 (2012).
14. M. S. Bhat, D. R. Poirer, and J. C. Heinrich, *Metall. Mater. Trans. B*, **26B**, 1049 (1995).
15. Konrad-Zuse-Zentrum fur Informationstechnik Berlin (ZIB), Germany and FEI, SAS, Avizo 9 User's Guide (2015).
16. D. Noble, E. Newren, and J. Lechman, *Int. J. Numer. Meth. Fl.*, **63**, 725 (2010).
17. CUBIT 15.0 User Documentation (2015).
18. J. R. Stewart and H. C. Edwards, Proceedings of the First Sandia Workshop on Large-Scale PDE-Constrained Optimization, Springer (2002).
19. H. C. Edwards and J. R. Stewart, Proceedings of the First MIT Conference, Cambridge, MA (2001).
20. I. Scribner Associates, Software downloads: ZPlot and ZView, Online (2015).
21. E. Barsoukov and J. R. Macdonald, *Impedance Spectroscopy: Theory, Experiment, and Applications*, p. 1, John Wiley & Sons, Inc., Hoboken, NJ (2005).